Article

Thermal Annealing and Phase Transformation of Serpentine-like Garnierite

Arun Kumar[1,2], Michele Cassetta[1], Marco Giarola[3], Marco Zanatta[4], Monique Le Guen[5], Gian Domenico Soraru[6], Gino Mariotto[1,*]

[1]Department of Computer Science, University of Verona, 37134, Verona, Italy
[2]CNR-Institute for Microelectronics and Microsystems, Agrate Brianza, 20864, Agrate, Italy
[3]Centro Piattaforme Tecnologiche (CPT), University of Verona, 37134, Verona, Italy
[4]Department of Physics, University of Trento, 38123, Povo, Trento, Italy
[5]Mining Division, ERAMET, 78190, Trappes, France
[6]Department of Industrial Engineering, University of Trento, 38123, Povo, Trento, Italy
*Correspondence: gino.mariotto@univr.it

Abstract: This study deals with vibrational and crystallographic aspects of the thermally induced transformation of serpentine-like garnierite into quartz, forsterite, and enstatite occurring at about 620 °C. Powder specimens of garnierite have been annealed in static air between room temperature and 1000 °C. The resulting products from the transformations detected based on thermogravimetric and differential thermal analysis, have been extensively characterized via microRaman spectroscopy, and X-ray diffraction. Our study shows that serpentine-like garnierite consists of a mixture of different mineral species. Furthermore, these garnierites and their composition can provide details based on the mineralogy and the crystalline phases resulting from the thermal treatment.

Keywords: Garnierite, Phase transformation, TGA/DSC, XRD, micro Raman spectroscopy

1. Introduction

In 1863, Jules Garnier discovered a nickel ore in New Caledonia, a magnesium-based nickel silicate later named as Garnierite [1]. Garnierite is mined from laterite deposits, and it is formed by weathering and secondary mineralization of igneous ultra-mafic rocks. Garnierite with the serpentine group of minerals is generally a mix of various Ni and Ni-Mg layer silicates [2-4]. However, there has always been difficulty in the identification of the garnierite minerals [1,5,6], as these minerals are poorly crystalline, naturally fine-grained nature as well as their frequent occurrence as mixtures of serpentine, talc, chlorite, sepiolite, and smectite minerals. Further, it has been shown that Ni^{2+} can substitute for Mg^{2+} in the serpentinite mineral lizardite since the two cations have similar ionic radii [2,7]. Because of their fine-grained, inhomogeneous distribution and their generally poor crystalline order, garnierite would seem to be very appropriate materials for characterization. However, if the initial minerals are mixtures of hydrous silicates, the phase development will depend on the distribution of nickel inside the mineral, they transform independently. Thus, the thermal transformations of garnierite are of interest for studying the primary nature of the minerals [8,9]. Furthermore, the thermal decomposition of these hydrous silicates provides insight about the thermal stability of garnierite. This is an important tool for the assessment of these types of materials in terms of mineral chemistry and shed a light on the amount of water on their structure [5], that has been confirmed very insightful to differentiate among the serpentine minerals [5,8,9].

In this study, thermal analysis has been applied to the study of the structural transformation of garnierite powder, which was unraveled by means of X-ray diffraction (XRD) and micro-Raman spectroscopy. In particular, microRaman spectroscopy constitutes a very powerful and in the meanwhile not invasive tool for mineral phase identification in geological samples, as well as in the characterization of the heterogeneous materials in

terms of component phases [10-13]. It has been employed here to investigate both the serpentine-like garnierite and its thermal phase transformation, which is not reported in previous studies.Therefore, the results of the present study can be compared only with the published literature using XRD analysis to study phase transformation of garnierite [14].

2. Materials and Methods

A garnierite sample (labeled as GN) coming from a mine of New Caledonia, was provided by ERAMET RESEARCH GROUP within the EU-H2020 SOLSA project grant no. 689868 (http://www.solsa-mining.eu), funded within the EU-H2020 Raw Material program. The sample was quite hard and compact rock, grey/brown colored, of irregular form, and some cm in size. For this study, some pieces of the solid rock were grinded manually using the mortar pestle to a finely grounded powder. The optical image of the sample taken with a high-quality camera is shown in Fig. 1.
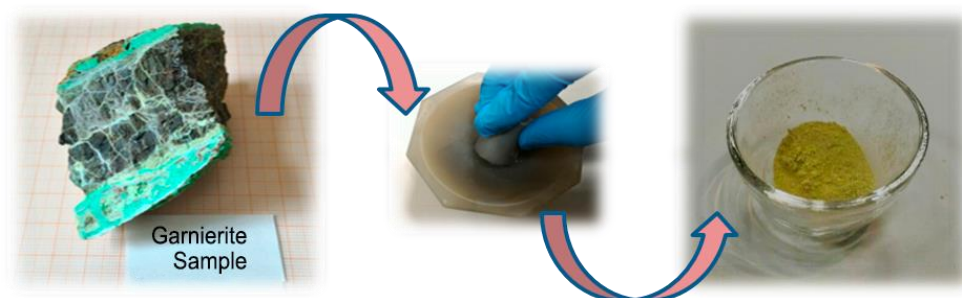

Figure 1. Optical image of the garnierite sample.

The thermal stability of the garnierite powder sample was investigated by differential scanning calorimetry (DSC) and thermogravimetric analysis (TGA) using an STA 449C Jupiter® analyzer (Netzsch-Gerätebau GmbH, Selb, Germany) from room temperature to 1000 °C at a heating rate of 5 °C min^{-1} and a static air flux of 40 ml min^{-1}. For TGA, 50 mg garnierite powder was measured along with a reference sample of aluminum powder.

The mineral characterization of the pristine and treated powders was done by means of XRD and micro-Raman spectroscopy.
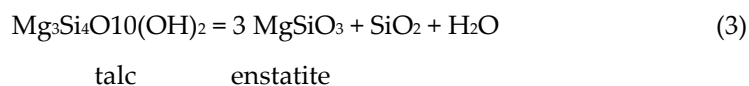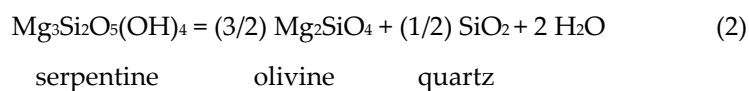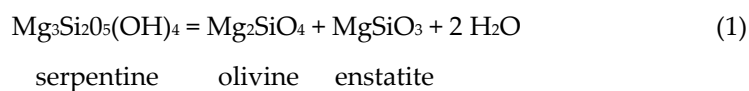
XRD measurements were acquired with a Thermo ARL X'TRA powder diffractometer, operating in the Bragg-Brentano geometry and equipped with a Cu-anode X-ray source (K$_\alpha$, λ = 1.5405 Å), using a Peltier Si(Li) cooled solid-state detector. The patterns were collected with a scan step of 0.03° in the 10-70 2θ range. Before the XRD measurements, the diffractometer was calibrated with a reference silicon powder (d$_{111}$ = 3.1353 Å).

Micro-Raman spectra were acquired in backscattering geometry with Horiba Jobin Yvon, LabRAM (HR800) spectrometer equipped with a 632.8 nm He-Ne laser and an optical microscope (Olympus, BX41). The laser beam was narrowed and focused through a 75-µm entrance pinhole and an 80x long working distance objective having 0.75 NA yielding a spatial resolution of about 1 µm and an irradiation power of 1.5 mW at the sample surface. The scattered light were dispersed using a grating with 600 lines/mm and collected with a Si-based CCD (charge-coupled device) detector of 1024 × 256 pixels cooled with liquid nitrogen. A composite spectrum covering the spectral range between 150 cm^{-1} and 4000 cm^{-1} was obtained by using the LabSpec (version 5) software package that merges several spectra with different wavenumber ranges by averaging the spectral intensities in the overlapping regions. Before performing measurements, the spectrometer was calibrated by using the 520.4 cm^{-1} peak of crystal Si.

3. Results and Discussion

The thermogravimetric analysis of the serpentine type garnierite, weight loss curve, and the phases formed at the various temperatures as presented in Fig. 2. Optimum loss of hydration water is observed at 40-90 °C (first endothermic peak on DTA curves).

Optimum temperatures of dihydroxylation of the layered silicates occur at 560-645 °C for the 7 Å- type (second endothermic peak) and 815-825 °C for the 10 Å - type (third endothermic peak), as already reported in the literature [7,15] for Ni-rich 'garnierite' veins, serpentine-like as well as serpentine + talc-like, respectively. This garnierite sample shows three distinct weight loss percentages; the first one is a continuous weight loss of about 3% from room temperature to up to 500 °C. The second one is a well-observed weight loss of about 5.5% at 620 °C, well known as an endothermic peak and the third one is of about 1.5% at 813 °C, which is well defined as an exothermic peak. The endothermic peak at 620 °C is assigned to the de-hydroxylation of the Ni incapacitated serpentine. After the de-hydroxylation at 620 °C, the anhydrous garnierite like serpentine breakdown and formation of anhydrous silicates crystals (olivine, enstatite) at 813 °C occurs. Further, the well-established mechanism of thermal transformation for the equilibrium of serpentine and talc [8,15,16] are shown below:

$$Mg_3Si_2O_5(OH)_4 = Mg_2SiO_4 + MgSiO_3 + 2\ H_2O \qquad (1)$$

$$\quad\ \text{serpentine} \qquad \text{olivine} \quad \text{enstatite}$$

$$Mg_3Si_2O_5(OH)_4 = (3/2)\ Mg_2SiO_4 + (1/2)\ SiO_2 + 2\ H_2O \qquad (2)$$

$$\quad\ \text{serpentine} \qquad\qquad \text{olivine} \qquad\quad \text{quartz}$$

$$Mg_3Si_4O_{10}(OH)_2 = 3\ MgSiO_3 + SiO_2 + H_2O \qquad (3)$$

$$\qquad \text{talc} \qquad\qquad \text{enstatite}$$

It was shown that up to 900 °C the serpentine mainly forms olivine but if it serpentine-like garnierite with low Ni content, up to this temperature, it will transform mainly into olivine but possibly also enstatite as shown in equation (1). But, if the content of Ni is high, it gives two main phases, olivine (forsterite) and quartz as shown in equation (2). Further, for talc-like garnierite, with low Ni content, the phase transformation gives rise to enstatite as shown in equation (3), whereas, with high Ni content it transforms into olivine phase up to the same range of temperature. From the above well-established literature in this type of minerals, we were able to demonstrate that our material is basically, serpentine-like garnierite with low Ni contents, which upon thermalization up to 900 °C transforms into olivine (forsterite), and small segregation of enstatite was also observed. However, the presence of quartz was already there in the initial mixture, and it was reported that the phase transformation depends on the initial minerals mixtures, and the distribution of nickel between the components, gives rise to transform them individually [8], which completely fit our results with XRD and microRaman spectroscopy.
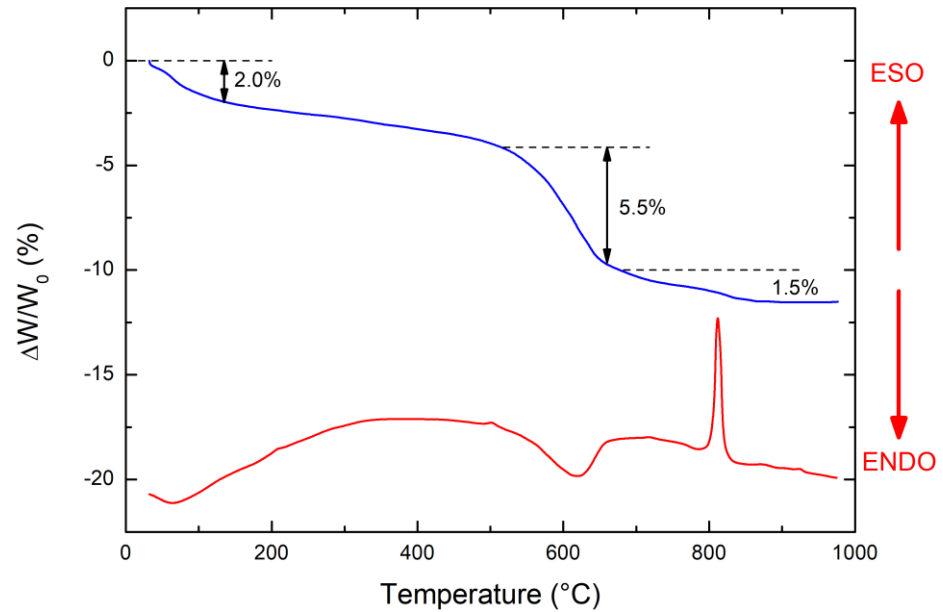
Figure 2. TGA curves of the pristine garnierite powder sample.

The above-mentioned phase transformation scenario is confirmed by microRaman and XRD measurements on both pristine or and treated powders.

Micro-Raman spectra of the pristine material show three major mineral phases, i.e. quartz and two Mg-Ni hydrous silicates. Typical spectra are reported in Fig. 3, where we highlighted the low wavenumber (150-1100 cm^{-1}) and the high-wavenumber (3550-3950 cm^{-1}) regions.
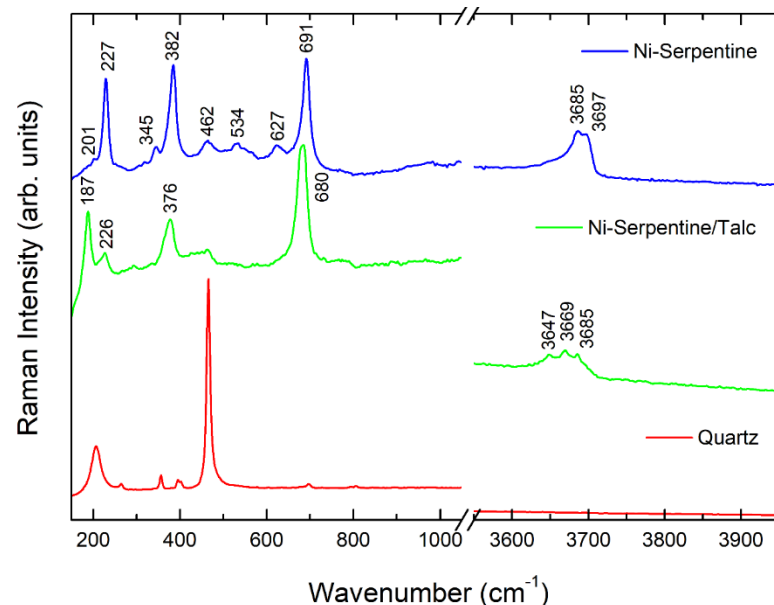

Figure 3. Micro Raman spectra of the pristine serpentine-like garnierite.

Quartz was found to be one of the major phases and its Raman spectrum is displayed in Fig. 3 (red line). The strong narrow peak observed at 464 cm^{-1}, together with the band centered at about 207 cm^{-1} and the small peak occurring at about 356 cm^{-1}, are the finger-prints of quartz [17-19]. Raman spectra of serpentine-like garnierites (Ni-Serpentine) are characterized by the presence of strong Raman bands at about 227 cm^{-1}, 382 cm^{-1}, and 691 cm^{-1} (Fig. 3, blue line). The peaks at about 227 and 382 cm^{-1} can be assigned to either serpentine group minerals or talc. These peaks are less intense (or even absent) when the garnierite contains high amounts of kerolite-pimelite [20]. In the literature, the band at 227 cm^{-1} is attributed to either metal-oxygen [19], or O-H-O vibrations [21,22]; whereas the peak at about 345 cm^{-1} and 382 cm^{-1} to metal-oxygen [23], SiO$_4$ bending/symmetric [21,22],

and the one at about 689 to Si-O vibrations [21-23], in all serpentine minerals. The spectrum of talc (Fig. 3, green line) shows a strong band peaked at about 680 cm^{-1}, but the other intense bands shown by Ni-serpentine are absent. In contrast, it shows intense bands at around 187 cm^{-1}; and a strong peak at 376 cm^{-1}.

The Si-O vibrational modes are particularly interesting since they are present in all the garnierite types originating a strong peak at about 691 cm^{-1} in serpentine-like garnierite and a band at about 680 cm^{-1} in talc-like one. Therefore, the shift of this Raman band can be used to discriminate between the two types of minerals [21-25]. As for the low-frequency region, the effect of the Ni content of Ni-bearing phyllosilicates is not easy to distinguish. The effect of the cations in the octahedral site and the Raman band positions below 600 cm^{-1} in phyllosilicates is well discussed in the literature [26]. Ni content in phyllosilicates may have a characteristic Raman Effect on the garnierite patterns. However, upon comparing the garnierite spectra with the crystalline, Ni-free serpentine, and talc ones no significant differences were observed at low frequency [5]. Conversely, the spectral region above 3500 cm^{-1} provides very interesting structural insights about the serpentine minerals. In fact, serpentine-like garnierites (Ni-Serpentines) shows a broad spectral feature consisting of a strong band centered at about 3685 cm^{-1} and of a pronounced shoulder peaked at 3697 cm^{-1}. In talc-like garnierite, a broader feature, consisting of three spectral components, peaked at about 3647 cm^{-1}, 3669 cm$^{-1,}$ and 3685 cm^{-1} respectively, is observed (see Figure 3, middle spectrum). All these bands are often assigned in the literature to O-H stretching or OH vibration of phyllosilicates [23-29]. The number and types of O-H sites and the types of cation occupancies around O-H groups control the number of O-H peaks, their positions, and their relative intensities [19]

Figure 4(a) shows the XRD pattern of natural serpentine-like garnierite powder. The garnierite powder is heterogeneous as expected and consists of different crystalline phases. The broad diffraction peak at 2θ=12.01° shows that the main Ni-bearing mineral phase is serpentine [(Mg, Fe, Ni)$_6$Si$_4$O$_{12}$(OH)$_6$] having d_{101} = 7.36 Å [7,30,31]. XRD results reveal that the diffraction peaks of serpentine-like garnierite dominate over the quartz peaks with respect to the concentration of Ni particles. The XRD pattern of quartz shows the major diffraction peaks at about 20.77°, 26.55°, 36.47°, 39.37°, 42.37°, 50.04°, 59.84° (degree) having d-spacing 4.27, 3.35, 2.46, 2.28, 2.13, 1.82, 1.54 Å respectively which are in well match with RRUFF database [32].
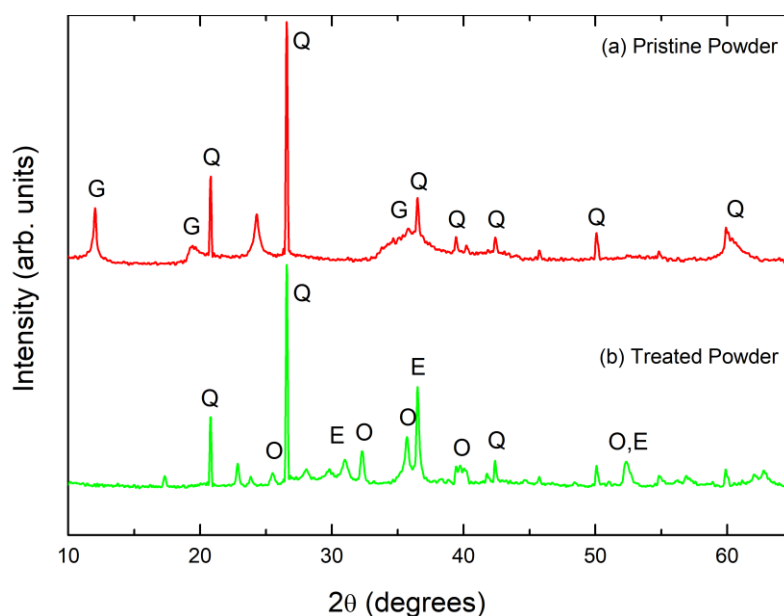

Figure 4. (a) Diffraction patterns of the pristine garnierite powder, (b) thermally treated powder together with patterns. Reflections marked G, Q, O, E indicates garnierite, quartz, olivine, and enstatite, respectively.

Thermally treated garnierite powder shows the presence of quartz peaks that progressively become sharper and better defined as shown in Fig. 4(b). Another major change observed and is the degradation of the Bragg peaks of serpentine minerals at about 36°, 42°, and 52.2° and their replacement by small reflections or shoulders upon thermalization. Specifically, the sharp overlapping reflections originating the broad band at about 2θ=36.2° for the untreated mixed serpentines (i.e.: 2.45 Å for chrysotile-2M, 2.51 Å for lizardite-1T, and 2.55 Å for antigorite) tend to wane and to be replaced by a broad two-dimensional diffraction band of olivine (forsterite) and enstatite (see Fig. 4), indicating a high degree of stacking disorder in silicate layers [15,16,30,31]. The obtained results advocate the close relationship of silicate layer minerals of small particle size and high crystal-defect density (broad reflections) with rests of well-crystallized serpentine species (sharp reflections) for the 7 Å- type layer silicates. These results indicate that the phase transformation of the garnierite to the olivine (forsterite) and enstatite has occurred and they are in good agreement with the previously reported literature [8,16]. This phase transformation from garnierite to olivine (forsterite) and enstatite is also evidenced by micro-Raman spectroscopy, see Fig. 5.
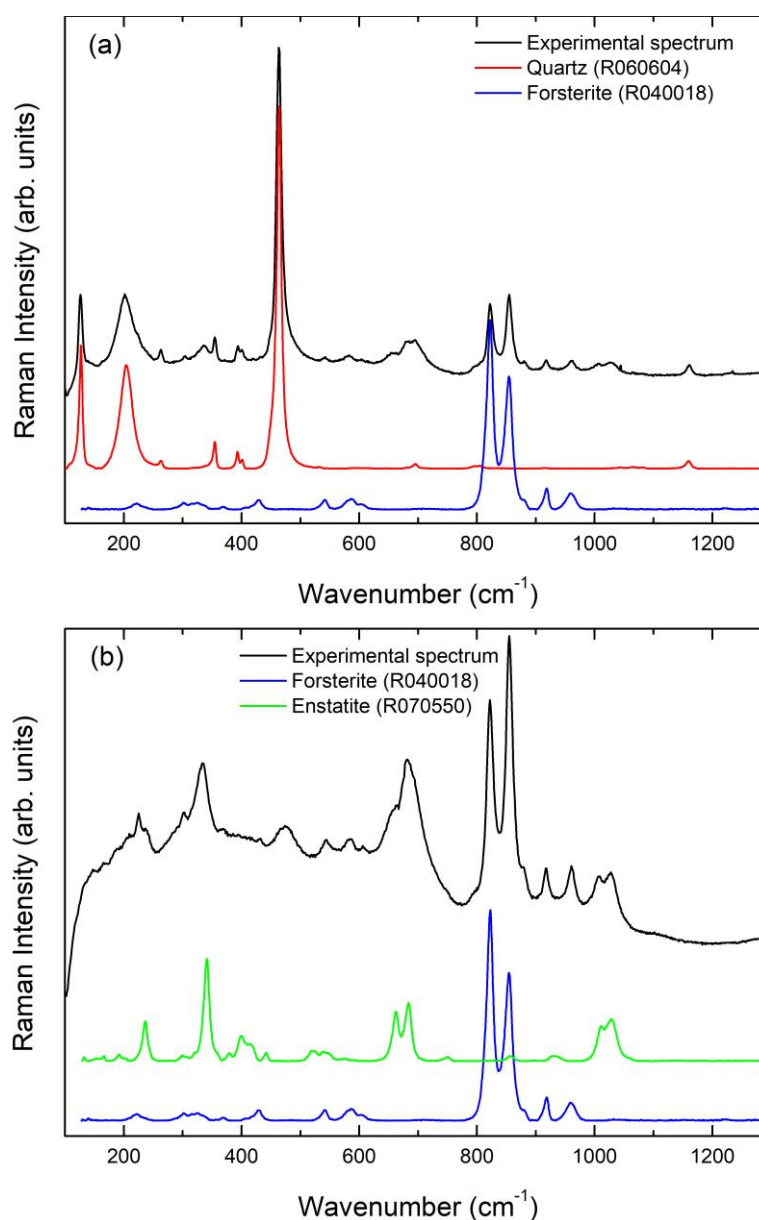

Figure 5. Typical Raman spectra of the thermally treated garnierite powder. RRUFF reference spectra used for phase identification are also reported.

In fact, the presence of quartz, olivine (forsterite), and enstatite in our treated sample is revealed by the occurrence of specific fingerprints in the Raman spectra collected from several surface micro-regions. An extensive investigation on the treated sample surface by micro Raman mostly quartz (α-SiO$_2$) with inclusions of olivine (forsterite Mg$_2$(SiO$_4$) and with micro-segregation of enstatite (MgSiO$_3$). The high spatial resolution of micro Raman allows selecting different grains obtaining spectra where the contribution of quartz and olivine (forsterite) is dominant along with micro inclusion of enstatite. The recorded Raman spectra were analyzed in terms of the different component phases with the help of both the RRUFF database [32-34] and the Raman Open Database [35-38]. However, spectra of a single-phase are seldom detected except for quartz. The experimental spectrum reported in Figure 5(a) originates mainly from quartz, being dominated by a very strong band peaked at about 464 cm^{-1} and two weak bands appear at about 127 cm^{-1} and 203 cm^{-1}, respectively. The characteristic band at 464 cm^{-1} corresponds to the vibrational mode of A1 symmetry [17-19]. At numerous investigation points, the presence of olivine (forsterite) along with quartz is detected through the observation of experimental spectra very similar to that of Figure 5(a).

Raman spectra of core olivine (forsterite) show two distinct bands at about 822 cm^{-1} and 854 cm^{-1} that define the Si-O symmetric stretching band and the Si-O antisymmetric stretching band, respectively [39-41]. In addition to these two main peaks other less intense Raman bands in forsterite occur at approximately 224 cm^{-1}, 303 cm^{-1}, 433 cm^{-1}, 542 cm^{-1}, 582 cm^{-1}, 603 cm^{-1}, 881 cm^{-1}, and 962 cm^{-1}.

In some cases, besides these typical phases, the occurrence of enstatite was also pointed out with the help of the RRUFF database [34]. The bottom spectrum of Figure 5(b) is the typical Raman spectrum of enstatite with the characteristic bands peaked at about 343 cm^{-1}, 662 cm$^{-1,}$ and 684 cm^{-1} [42,43] which clearly matches the experimental data. On the other hand, Figure 5(b) shows a spectrum, where the contribution of olivine (forsterite) is dominant over enstatite. In general, Raman spectra recorded from the treated powders show the co-existence of two or more phases, which turn out in fair agreement with those detected by XRD.

5. Conclusions

Our experimental results suggest the occurrence of an important thermally induced transformation of serpentine-like garnierite from New Caledonia in terms of crystallographic, microstructural, and phase changes which result in olivine (forsterite) and enstatite as the most abundant mineral phases. Thermogravimetric analysis proves there are at least four decomposition steps attributed to dehydration, dihydroxylation, and decomposition of the formed phases. The mechanism for the thermal decomposition of garnierite is highlighted. Serpentine-like garnierite transforms between 800-1000 °C depending on their NiO content. Serpentine-like garnierite, with low NiO content, transform mainly to an olivine phase. The formation of olivine and enstatite as a result of the thermal annealing of garnierite is supported both by XRD and microRaman spectroscopy results. These results may help to classify mixed crystalline phases in the initial minerals.

Author Contributions: Conceptualization, A.K. and M.Z.; methodology, A.K.; validation, A.K., M.Z. and G.M.; XRD, M.G.; TGA/DSC, G.D.S.; writing-original draft preparation, A.K.; writing-review and editing, M.C.; project administration, M.L.G.; supervision, G.M.; All authors have read and agreed to the published version of the manuscript.

Conflicts of Interest: The authors declare no conflict of interest.

References

1. Xiao, J.; Ding, W.; Peng, Y.; Chen, T.; Zou, K.; Wang, Z. Extraction of nickel from garnierite laterite ore using roasting and magnetic separation with calcium chloride and iron concentrate. Minerals 2020, 10, 352.

2. Qu, T.; Tian, Y.; Yang, B.; Liu, D.C.; Xu, B.Q.; Dai, Y.N. Study on the thermodynamic and experimental carbothermic reduction of garnierite. In Magnesium Technology; Minerals, Metals and Materials Society 2012; pp. 505–510 ISBN 9781118291214.

3. De Bakker, J.; Peacey, J.; Davis, B. Thermal decomposition studies on magnesium hydroxychlorides. Can. Metall. Q. 2012, 51, 419–423.

4. Mongelli, G.; Taghipour, B.; Sinisi, R.; Khadivar, S. Mineralization and element redistribution in the Chah-Gheib Ni-laterite ore zone, Bavanat, Zagros Belt, Iran. Ore Geol. Rev. 2019, 111, 102990.

5. Villanova-de-Benavent, C.; Jawhari, T.; Roqué-Rosell, J.; Galí, S.; Proenza, J.A. Ni-bearing phyllosilicates ("garnierites"): New insights from thermal analysis, μRaman and IR spectroscopy. Appl. Clay Sci. 2019, 175, 47–66.

6. Cathelineau, M.; Quesnel, B.; Gautier, P.; Boulvais, P.; Couteau, C.; Drouillet, M. Nickel dispersion and enrichment at the bottom of the regolith: formation of pimelite target-like ores in rock block joints (Koniambo Ni deposit, New Caledonia). Miner. Depos. 2016, 51, 271–282.

7. Wells, M.A.; Ramanaidou, E.R.; Verrall, M.; Tessarolo, C. Mineralogy and crystal chemistry of "garnierites" in the Goro lateritic nickel deposit, New Caledonia. Eur. J. Mineral. 2009, 21, 467–483.

8. Hang, Pham Thi. Brindley, G.W. THE NATURE OF GARNIERITES--III THERMAL TRANSFORMATIONS. Clays Clay Miner. 1973, 21, 51–57.

9. Sazama, U.; Reller, A. The thermochemical reactivity of silicate minerals in hydrogen and methane. J. Therm. Anal. 1996, 47, 357–364.

10. Duée, C.; Maubec, N.; Laperche, V.; Capar, L.; Bourguignon, A.; Bourrat, X.; Yassine, B.; Mendili, E.; Chateigner, D.; Gascoin, S.; et al. Combined mineralogy and chemistry on drill cores: challenging for on-line-real-time analyses. In Proceedings of the Mineral Resources to Discover; Proceedings of the 14th Biennial SGA Meeting: Quebéc, Canada, 2017; Vol. 3, pp. 1241–1244.

11. Secchi, M.; Zanatta, M.; Borovin, E.; Bortolotti, M.; Kumar, A.; Giarola, M.; Sanson, A.; Orberger, B.; Daldosso, N.; Gialanella, S.; et al. Mineralogical investigations using XRD, XRF, and Raman spectroscopy in a combined approach. J. Raman Spectrosc. 2018, 49, 1023–1030.

12. El Mendili, Y.; Chateigner, D.; Orberger, B.; Gascoin, S.; Bardeau, J.F.; Petit, S.; Dueé, C.; Le Guen, M.; Pilliere, H. Combined XRF, XRD, SEM-EDS, and Raman Analyses on Serpentinized Harzburgite (Nickel Laterite Mine, New Caledonia): Implications for Exploration and Geometallurgy. ACS Earth Sp. Chem. 2019, 3, 2237–2249.

13. Duée, C.; Orberger, B.; Maubec, N.; Laperche, V.; Capar, L.; Bourguignon, A.; Bourrat, X.; El Mendili, Y.; Chateigner, D.; Gascoin, S.; et al. Impact of heterogeneities and surface roughness on pXRF, pIR, XRD and Raman analyses: Challenges for on-line, real-time combined mineralogical and chemical analyses on drill cores and implication for "high speed" Ni-laterite exploration. J. Geochemical Explor. 2019, 198, 1–17.

14. Brindley, G.W.; Thi Hang, P. The nature of garnierites -I structures, chemical compositions and color characteristics. Clays Clay Miner. 1973, 21, 19–26.

15. Brindley, G. W. Hayami, R. Kinetics and Mechanisms of Dehydration and Recrystallization of Serpentine*—I. Clays Clay Miner. 1963, 12, 35–47.

16. Brindley, G. W. Hayami, R. Mechanism of formation of forsterite and enstatite from serpentine. Mineral. Mag. 1965, 189–195.

17. Scott J.F. and Porto S.P.S. Longitudinal and Transverse Optical Lattice Vibrations in Quartz. Phys Rev (1967), 161, 903-910.

18. Shapiro, S.M.; O'Shea, D.C.; Cummins, H.Z. Raman scattering study of the alpha-beta phase transition in quartz. Phys. Rev. Lett. 1967, 19, 361.

19. Schmidt, P.; Bellot-Gurlet, L.; Leá, V.; Sciau, P. Moganite detection in silica rocks using Raman and infrared spectroscopy. Eur. J. Mineral. 2014, 25, 797–805..

20. Wang, A.; Freeman, J.J.; Jolliff, B.L. Understanding the Raman spectral features of phyllosilicates. J. Raman Spectrosc. 2015, 46, 829–845.

21. Rinaudo, C.; Gastaldi, D.; Belluso, E. Characterization of chrysotile, antigorite and lizardite by FT-Raman spectroscopy. Can. Mineral. 2003, 41, 883–890.

22. Groppo, C.; Rinaudo, C.; Cairo, S.; Gastaldi, D.; Compagnoni, R. Micro-Raman spectroscopy for a quick and reliable identification of serpentine minerals from ultramafics. Eur. J. Mineral. 2006, 18, 319–329.

23. Kloprogge, J.T.; Frost, R.L.; Rintoul, L. Single crystal Raman microscopic study of the asbestos mineral chrysotile. Phys. Chem. Chem. Phys. 1999, 1, 2559–2564.

24. Blaha, J.J.; Rosasco, G.J. Raman Microprobe Spectra of Individual Microcrystals and Fibers of Talc, Tremolite, and Related Silicate Minerals. Anal. Chem. 1978, 50, 892–896.

25. Rosasco, G.J.; Blaha, J.J. RAMAN MICROPROBE SPECTRA AND VIBRATIONAL MODE ASSIGNMENTS OF TALC. Appl. Spectrosc. 1980, 34, 140–144.

26. Wang, A.; Freeman, J.; Kuebler, K.E. Raman Spectroscopic Characterization of Phyllosilicates. In Proceedings of the Lunar and Planetary Science XXXIII; 2002; pp. 1374.

27. Auzende, A.L.; Daniel, I.; Reynard, B.; Lemaire, C.; Guyot, F. High-pressure behaviour of serpentine minerals: A Raman spectroscopic study. Phys. Chem. Miner. 2004, 31, 269–277.

28. Frost, R.L.; Reddy, B.J.; Dickfos, M.J. Raman spectroscopy of the nickel silicate mineral pecoraite - An analogue of chrysotile (asbestos). J. Raman Spectrosc. 2008.

29. Cathelineau, M.; Caumon, M.-C.; Massei, F.; Brie, D.; Harlaux, M. Raman spectra of Ni-Mg kerolite: effect of Ni-Mg substitution on O-H stretching vibrations. J. Raman Spectrosc. 2015, 46, 933–940.

30. Zevgolis, E.N.; Zografidis, C.; Perraki, T.; Devlin, E. Phase transformations of nickeliferous laterites during preheating and reduction with carbon monoxide. J. Therm. Anal. Calorim. 2010, 100, 133–139.

31. Fritsch, E.; Juillot, F.; Dublet, G.; Fonteneau, L.; Fandeur, D.; Martin, E.; Caner, L.; Auzende, A.-L.; Grauby, O.; Beaufort, D. An alternative model for the formation of hydrous Mg/Ni layer silicates ('deweylite'/'garnierite') in faulted peridotites of New Caledonia: I. Texture and mineralogy of a paragenetic succession of silicate infillings. Eur. J. Mineral. 2016, 28, 295–311.

32. Quartz R060604 - RRUFF Database: Raman, X-ray, Infrared, and Chemistry Available online: https://rruff.info/quartz/display=default/R060604 (accessed on Nov 21, 2020).

33. Forsterite R040018 - RRUFF Database: Raman, X-ray, Infrared, and Chemistry Available online: https://rruff.info/forsterite/display=default/R040018 (accessed on Nov 21, 2020).

34. Enstatite R070550 - RRUFF Database: Raman, X-ray, Infrared, and Chemistry Available online: https://rruff.info/enstatite/display=default/R070550 (accessed on Nov 21, 2020).

35. El Mendili, Y.; Vaitkus, A.; Merkys, A.; Gražulis, S.; Chateigner, D.; Mathevet, F.; Gascoin, S.; Petit, S.; Bardeau, J.F.; Zanatta, M.; et al. Raman Open Database: first interconnected Raman–X-ray diffraction open-access resource for material identification. J. Appl. Crystallogr. 2019, 52, 618–625.

36. Raman Open Database: Information card for entry 3500272 Available online: https://solsa.crystallography.net/rod/3500272.html (accessed on Nov 21, 2020).

37. Raman Open Database: Information card for entry 3500271 Available online: https://solsa.crystallography.net/rod/3500271.html (accessed on Nov 21, 2020).

38. Raman Open Database: Information card for entry 3500029 Available online: https://solsa.crystallography.net/rod/3500029.html (accessed on Nov 21, 2020).

39. Lin, C.C. High-pressure Raman spectroscopic study of Co- and Ni-olivines. Phys. Chem. Miner. 2001, 28, 249–257.

40. Kolesov, B.A.; Geiger, C.A. A Raman spectroscopic study of Fe-Mg olivines. Phys. Chem. Miner. 2004, 31, 142–154.

41. Weber, I.; Böttger, U.; Pavlov, S.G.; Jessberger, E.K.; Hübers, H.W. Mineralogical and Raman spectroscopy studies of natural olivines exposed to different planetary environments. Planet. Space Sci. 2014, 104, 163–172.

42. Catalano, M.; Bloise, A.; Pingitore, V.; Cazzanelli, E.; Giarola, M.; Mariotto, G.; Barrese, E. Synthesis and characterization of Zn-doped enstatite. Appl. Phys. A Mater. Sci. Process. 2015, 120, 175–182.

43. Zucker, R.; Shim, S.H. In situ Raman spectroscopy of MgSiO3 enstatite up to 1550 K. Am. Mineral. 2009, 94, 1638–1646.